nature nanotechnology
SUPPLEMENTARY INFORMATION
https://doi.org/10.1038/s41565-017-0002-1

In the format provided by the authors and unedited.

Realization of ground state in artificial kagome spin ice via topological defect-driven magnetic writing

Jack C. Gartside[1*], Daan M. Arroo[1], David M. Burn[2], Victoria L. Bemmer[3], Andy Moskalenko[1], Lesley F. Cohen[1] and Will R. Branford[1]

[1]Blackett Laboratory, Imperial College London, London SW7 2AZ, UK. [2]Diamond Light Source, Didcot, OX11 0DE UK. [3]Department of Materials, Imperial College London, London SW7 2AZ, UK. *e-mail: j.carter-gartside13@imperial.ac.uk

© 2017 Nature America Inc., part of Springer Nature. All rights reserved.

Realisation of ground state in artificial kagome spin ice via topological defect-driven magnetic writing

J. C. Gartside[1]*, D. M. Arroo[1], D. M. Burn[2], V. L. Bemmer[3], A. Moskalenko[1], L. F. Cohen[1] and W. R. Branford[1]

Blackett Laboratory, Imperial College London[1]

Diamond Light Source, Didcot[2]

Department of Materials, Imperial College London[3]

September 12, 2017

Supplementary information

1 Micromagnetic dynamics of the topological defect-driven magnetic writing process

To gain further insight into the dynamics of the writing process, micromagnetic simulations were performed using OOMMF. To isolate the intrinsic MFM tip specific dynamics from the effects of the magnetic charges at the nanowire ends, a semi-infinite wire of 10 μm length was simulated with plates of fixed magnetisation employed at either end to effectively remove the magnetic charges [1]. A magnetic charge q_{tip} and associated monopolar H field representing the MFM tip were passed over a $75 \times 10\text{nm}^2$ cross-sectional wire at a tip-wire separation of 5 nm, locally distorting the spin system and introducing dynamic topological defects as described above. The time dependent separation between the two 180° DWs formed by these defects was measured for a range of q_{tip} values, with the results shown in figure S1 a). The tip first reaches the wire at $t = 2.5$ ns, soon after which the injected DWs are seen to rapidly separate. In the absence of magnetic wire-end charges the dipolar attraction between the two DWs eventually brings them back together, forming a stable composite 360° DW [2]. The peak inter-DW separation reached was found to monotonically increase with q_{tip}. To investigate the mechanism by which this increasing separation occurs, a method is required for quantifying the amount of potential energy being stored in the contorted high-energy DW during the injection process. The key micromagnetic terms governing such dynamics are the exchange and demagnetisation energies. In order to separate the energy cost of the stable, non-distorted DWs from the additional potential energy

*j.carter-gartside13@imperial.ac.uk

driving the DW separation, the combined exchange and demagnetisation energies were measured from OOMMF simulations relative to the energy of a stable 360° DW where the spin-chains of both composite 180° DWs lie in a straight, low-energy conformation perpendicular to the long-axis of the wire. Any increase in micromagnetic energy relative to this can be linked to the distortions induced in the spin-chains by H_{tip}, with a value of zero reached at the end of the injection process corresponding to the formation of a stable 360° DW. The time-evolution of the resultant composite energy, termed the 'excess micromagnetic energy', is plotted in fig. S1 b) for the same time period and q_{tip} values as fig. S1 a) with a matching colour scheme indicating q_{tip} for each curve. Time is presented on a logarithmic scale as the dynamics of interest occur in the initial stage of the injection process when the tip is close to the wire. Figure S1 b) shows an initial sharp increase in the excess micromagnetic energy as the vortex defect is introduced to the wire and the spin-chains are formed, peaking abruptly at $t = 3.2$ ns where the MFM tip finishes crossing the nanowire. At this point where the vortex defect decomposes and the DWs are no longer bound, the excess micromagnetic energy rapidly drops, coinciding with a large increase in the DW separation seen in fig. S1 a). This correlation serves as a good indication that the MFM tip is indeed inducing a large amount of micromagnetic potential energy in the nascent contorted DW, which is then converted to DW kinetic energy in the absence of the tip as the DW violently straightens out, generating momentum in the process.

To better understand the relationship between the excess micromagnetic energy and the momentum imparted to the dynamic DW, figure S1 c) plots the peak DW separation reached in fig. S1 a) against the peak micromagnetic energy from fig. S1 b). The diamond markers represent data extracted from the OOMMF simulations shown in fig. S1 a) with colour codes corresponding to the same q_{tip} values as in the previous two panels. A smooth monotonic increase in DW separation is observed with increasing excess micromagnetic energy, further suggesting that the release of pent-up micromagnetic potential is driving the DW separation. However, as micromagnetic dynamics are complex with multiple competing interactions present, it is not immediately clear that the excess micromagnetic energy is the dominant component driving the injection dynamics. In order to test whether the qualitative behaviour observed in the OOMMF simulations can be reproduced by considering just the excess micromagnetic energy, a simple semi-analytical model was employed, treating each 180° DW as a quasiparticle with effective mass $m = \frac{h^2 N}{4\pi^2 K \lambda^2}$ where N, K and λ represent the number of spins in the DW, the transverse magnetic anisotropy energy of the wire and the DW width respectively[3–5], and magnetic charge $2q_m$ where $q_m = \pm M_s w t$ with M_s, w and t being the saturation magnetisation, wire width and thickness respectively[6]. Here, values of $m = 3.41 \times 10^{-23}$ kg and $2q_m = 1.29 \times 10^{-9}$ Am were determined. The DW mass per unit area is $m_{area} = 2.56 \times 10^{-20}$ kg/nm^2. The two opposite magnetic charge polarity DWs are confined to a one-dimensional line representing the nanowire at an initial separation r_0, measured from the OOMMF simulations at the moment the vortex topological defect decomposes into half-vortex defects and the DWs become unbound. One DW remains fixed at $r = 0$, representing the low-energy DW formed from the straight spin-chain, while the other representing the high-energy DW formed from the contorted spin-chain is initialised moving away from $r = 0$ with a velocity v_0 given by converting the peak excess micromagnetic energy (taken from OOMMF at the point the tip-localised vortex defect decomposes) to kinetic energy via $\frac{1}{2}mv_0^2$. The moving DW feels an attractive magnetic Coulomb force $F_{DW} = \frac{\mu_0}{4\pi r^2}(2q_m)^2$ directed towards the static DW at $r = 0$ and a viscous Gilbert-damping drag force[7] $F_{drag} = -vb$ where b is a phenomenological damping coefficient, here 1.53×10^{-14} Nsm^{-1}. The equation of motion for the moving DW is

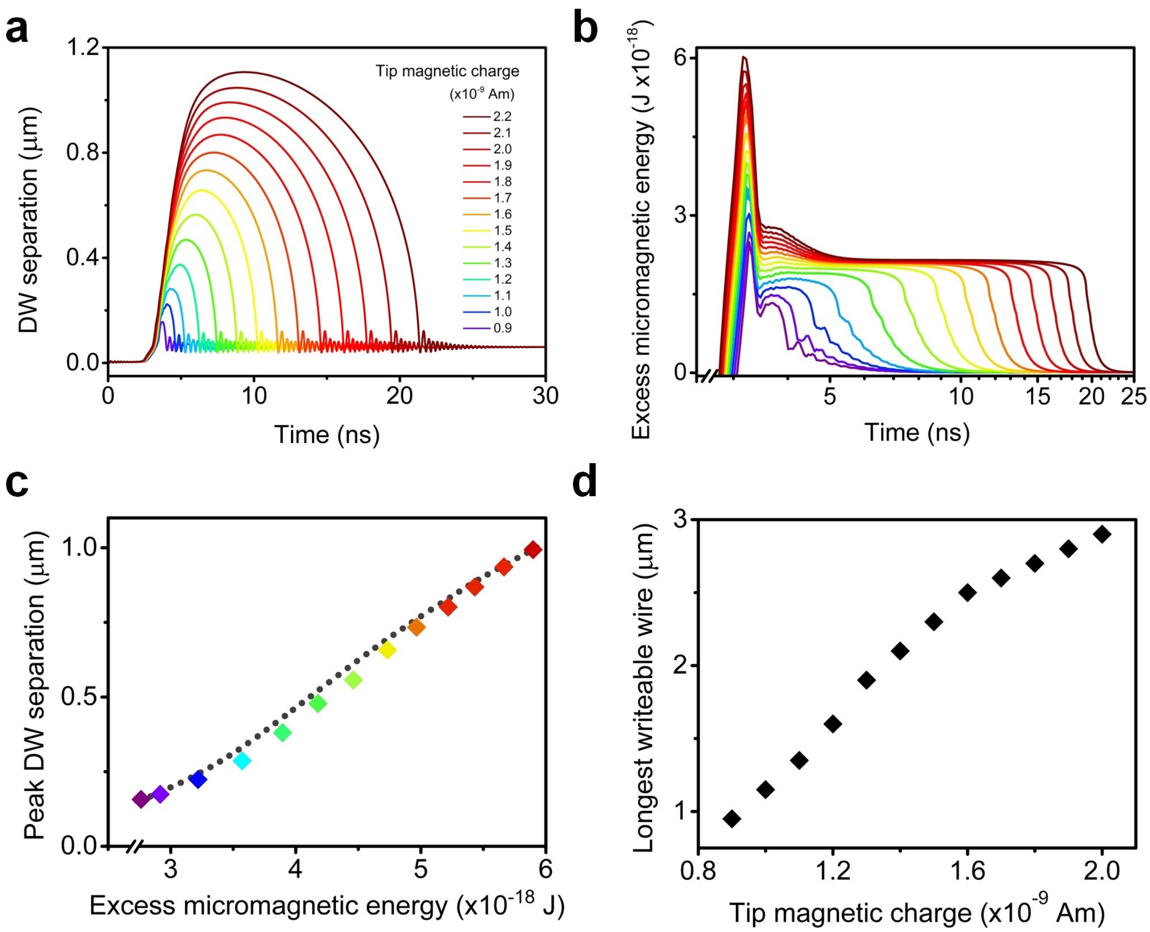

Figure S1: Dynamics of the TMW writing process.

a) Time-dependent separation between domain walls injected in an infinite 75 nm wide nanowire by varying strength MFM tips. Tip reaches the wire at $t = 2.5\ ns$.

b) Excess micromagnetic energy versus time with colours corresponding to the same range of tip strengths as a). **c)** Peak inter-DW separation for different strength MFM tips as a function of peak excess micromagnetic energy. Coloured diamonds are data taken from the OOMMF simulations shown in panel a) with colours corresponding to the same tip strengths. Grey dotted line shows data given by a simple semi-analytical kinematic model.

d) Longest simulated TMW-switchable nanowire versus MFM tip magnetic charge strength q_{tip}.

then solved for DW position r at each time step $\delta t = 1$ ps using numerical integration. The results of this model are plotted in figure 2 b) of the main manuscript as the dotted grey line and can be seen to closely reproduce the behaviour observed in the OOMMF simulations. This provides further evidence supporting our hypothesis that micromagnetic potential energy stored in the shape-distortion of the forming DW by H_{tip} is responsible for driving the momentum of the dynamic DW and therefore the writing process, rather like drawing back a pinball-machine plunger which is released once the tip completes its crossing of the wire. TMW injection on 'quasi-infinite' nanowire arrays was performed with subsequent MFM imaging supporting the dynamics observed in OOMMF, suggesting that the picture of one high-energy DW 'fired' down the wire and a second relatively static low-energy DW is indeed physically accurate. The results of this experiment are discussed below.

To now examine the writing dynamics of TMW in a finite-length wire with end charges present, simulations were performed on 10 nm $\times$ 75 nm cross-sectional wires of 0.5-3 μm length. As before, a magnetic charge and associated monopolar field representing the MFM tip were passed across the wire close to its central point. The topological defects and associated DWs were injected into the wire as described above, but for wires below a certain length threshold the dynamic DW now makes on contact with the wire end, unwinding to a smooth spin state before the remaining DW is pulled into the opposite end, also unwinding and leaving a collinear reverse-magnetised state. The longest reversible wire was determined for a range of q_{tip} values by simulating injection on increasingly longer wires until the DWs were no longer able to reach the wire ends and reversal did not occur. The relation between q_{tip} and the longest writeable wire is shown in fig. S1d), with a monotonic increase observed in maximum writeable wire length with increasing q_{tip} values. Wires several μm in length are switchable by q_{tip} values corresponding to typical high-moment MFM tips ($\sim 10^{-9}$ Am), matching well with experimentally observed behaviour. The trend between longest writeable wire and q_{tip} suggests that TMW may be tailored to switch wires of a desired length by selecting appropriate strength MFM tips, achieved practically by varying the thickness of the magnetic coating layer on the tip. Potentially allowing for longer wires to be written using thicker magnetic coatings ($>$ 60 nm) than are commercially available.

2 Detailed picture of domain wall formation process

The clearest framework to understand the underlying TMW mechanism invokes topological charge in a nanomagnetic context. For excellent foundational descriptions of this we refer the reader to the following works[8,9]. To illustrate the topological nature of the process we reiterate that the stray tip field H_{tip} is insufficient to switch bars by proximity alone - if the tip is held static above the bars no reversal will occur. The condition for a switching event is that the tip crosses both edges of the bar.

As mentioned in the 'Working principle of TMW' section in the main text, the locally monopolar tip field H_{tip} induces a vortex in the magnetisation under the apex of the tip when it reaches the nanowire[10,11]. In an otherwise smooth spin system, a vortex is a topological defect with an associated winding number[8] of +1. The net winding number of a ferromagnetic spin system is rigorously conserved to avoid discontinuities in the magnetisation and as such, the formation of the vortex is balanced by creating a pair of half-vortex topological defects with winding number -1/2. Defects with fractional winding number are forbidden in the bulk so the half-vortices remain bound

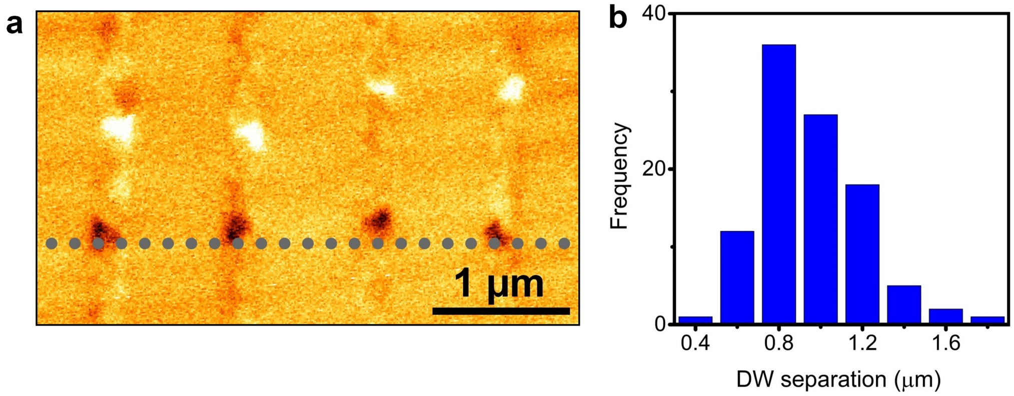

Figure S2: Results of TMW performed in 'quasi-infinite' nanowire arrays

a) MFM image of 100 nm × 10 nm cross-section Co nanowire array after TMW injection. Dotted grey line represents path of MFM tip during writing.

b) Histogram showing separation between injected DWs in nanowire arrays shown in a), measured over 101 TMW writing events.

to the structure edge[8]. The +1 vortex remains under the tip as it moves through the nanostructure, maintaining a connection to the edge-bound half-vortices via two continous chains of reversed spins to avoid a magnetisation discontinuity. The chains are highlighted in the t = 3.5 ns panel by the dotted grey line (left of tip) and the dashed white line (in line with tip motion). The tip effect is asymmetric: On one side (right of tip in fig. 1 b) the component of H_{tip} along the wire-length is parallel to the wire magnetisation, so any disturbance to the micromagnetic structure is minimal. On the other side H_{tip} is anti-parallel to the magnetisation and drives local magnetic reversal. This forces the left-hand chain into an elongated curve around a nascent left-magnetised domain created between the -1/2 defects (t = 3.5 ns) in the wake of the tip. As the tip finishes crossing the structure, the vortex is brought into contact with the structure's lower edge. Whole integer defects may only exist in the bulk, so the vortex decomposes into a pair of edge-bound +1/2 defects to conserve the net winding number[8]. The chains of reversed spins now each connect a +1/2 topological defect on the bottom edge of the structure to a corresponding -1/2 defect on the top edge (t = 5 ns). A 180° DW is defined as a bound pair of ±1/2 topological defects, hence each chain-defect pair constitues an independent 180° DW[8]. The rest of the TMW process does not require additional topological charge treatment to be understood, and continues with the unwinding of the left and right-hand DWs into the left and right ends of the wire as described in the main text.

3 Topological defect-driven magnetic writing in quasi-infinite nanowires

To ascertain whether the injection dynamics observed in micromagnetic simulation represent a realistic picture of the injection process, 'quasi-infinite' nanowires were experimentally fabricated. Arrays of 20 μm long nanowires were fabricated, such that at their central points the effects of the wire-end magnetic charges were negligible. The wires were initially magnetised along their long-axis by a global H field. TMW injection was then performed across the mid-point of the wires and the resultant state imaged via MFM, with Co used rather than NiFe as the harder magnetic material allows for non-invasive MFM imaging of DWs without H_{tip} disturbing them. A high deposition rate and coarse liftoff process were employed in an attempt to generate a high density of DW pinning sites in order to 'trap' DWs at various stages of the dynamic injection process. Fig. S2 a) shows a nanowire array after TMW injection. A dark contrast 180° DW is observed in each wire under the path of the tip, with a second, light contrast, 180° DW displaced 0.8-1.2 μm along the wire. In each case the light DW is displaced to the same side of the dark DW, in this case towards the top of the image frame. The observed behaviour correlates well with our simulation results. As shown in figure 1 b) of the main manuscript, we observe in simulation one DW forming in a high-energy contorted state (to the left of tip in fig. 1 b), t = 3.5 ns panel) which is then accelerated down the wire with the second DW remaining relatively static (fig. 1 b), t = 5 ns panel) as it formed in a low-energy state straight across the wire. The dark DWs remaining aligned along the dotted path of the tip correspond with the simulated behaviour of the low-energy DWs while the light DWs displaced along the wire from the tips path match the simulated behaviour of the high-energy DWs. It is important to note that the DWs imaged here have become pinned at some point during the injection process (the lowest-energy state being a stable 360° DW with around 90 nm separation between DWs), each wire represents an effective snapshot at a random point during the injection process and the DW separations can be taken as a minimum separation reached. Figure S2 b) is a histogram of DW separations, measured over 101 separate TMW injection events in the same nanowire shown in fig. S2 a). A separation range of of 0.44-1.66 μm is observed, corresponding well to the separations observed in OOMMF simulations and suggesting that dynamic topological defects induced by the tip are indeed responsible for the TMW writing process.

4 Additional states realised via topological defect-driven magnetic writing

To demonstrate the 'erase' functionality of TMW along with the ease by which complex states may be transitioned between, every macrospin in the spin-crystal ground state shown in fig. 3 b) of the main manuscript was reversed via TMW, preparing the alternate chirality ground state. Figure S3 a) shows a single TMW-switched bar in an otherwise complete ground state configuration. The remaining 29 macrospins were then reversed using TMW. Figure S3 b) showing the resultant alternate-chirality ground state, highlighting the accuracy and flexibility of the writing technique.

So far, all ASI considered has been formed of 1 μm long nanowires. This length was chosen for two reasons, to enable clear spatial resolution of individual magnetic charges during MFM imaging and to avoid confusion that our magnetic reversal process was just a conventional field-based switching event (the tip field decays away from the tip apex rapidly and is negligible across most of the 1 μm length). However, TMW still performs well at much smaller dimensions. Figure S4 shows a Py ASI array formed of 400 nm long nanowires with a range of TMW-written states including columns of +3 q_m vertices. Micromagnetic simulations were performed on even much smaller bars, with figures S5 and S6 showing TMW reversal of 60 nm wide and 30 nm wide nanowires of various length respectively. Controllable 180 ° magnetisation reversal was successfully performed down to dimensions of 32 nm by 30 nm by 10

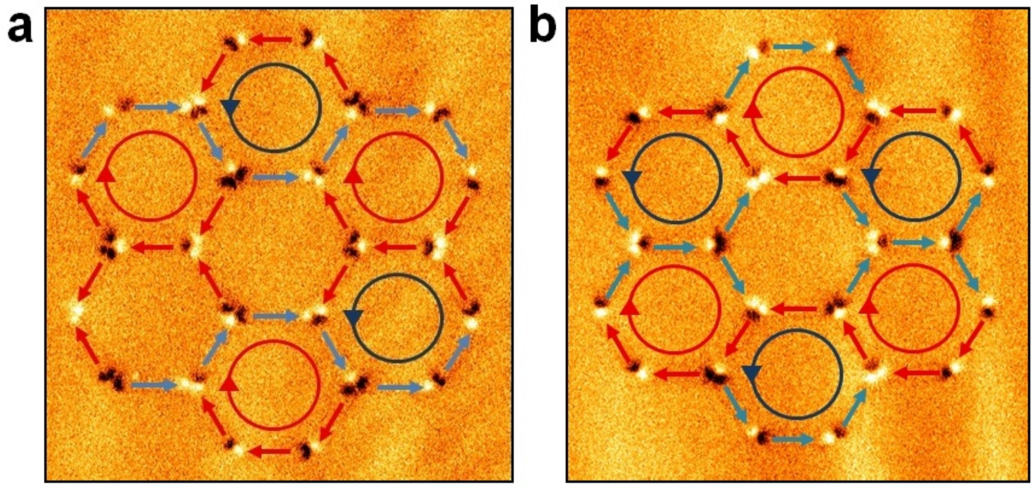

Figure S3: TMW-written states in disconnected ASI rosettes

a) MFM image of a single bar (bottom-left loop) reversed from an otherwise complete ground state, highlighting 'erase' functionality.

b) MFM image of alternate-chirality ground state. All 30 macrospins have been reversed from the original ground state.

nm. However, for lengths of below 90 nm the reversal process did not occur via the injection of well-formed DWs and increasingly resembles coherent Stoner-Wohlfarth rotation as the wire length is reduced.

New research initiatives in ASI and frustrated magnetism research are increasingly focusing on novel lattice geometries such as Shakti, pentagonal, 'Tetris' and brickwork designs[12–15]. The majority of these designs take a square or mixed square-hexagonal base lattice and remove selected bars to regularly vary the coordination number at vertices. To demonstrate TMW's capacity to function across a wide variety of lattice designs, micromagnetic simulations were performed on TMW writing of the highest possible energy $\pm 4\ q_m$ states in square-lattice ASI. Figure S7 shows the successful TMW creation of $\pm 4\ q_m$ vertex states in a two-vertex square ASI system comprising 400 nm × 60 nm × 10 nm Py bars. By demonstrating the ability to write the highest energy states into both square and hexagonal geometry ASI, TMW can be seen to retain its functionality across a host of lattice designs derived from these bases. We anticipate no difficulty with the use of TMW in more exotic geometries such as Penrose and other quasi-crystal designs.

5 Flexibility of topological defect-driven magnetic writing in systems containing a distribution of switching fields

As we have already seen, TMW removes the need for any uniformly applied external global fields. While this has the benefit of both simplifying the experimental setup and allowing integration with systems disrupted by applied fields, in the following section we show that removing the need for global fields is essential for any widely applicable magnetic writing technique. Global field based protocols using an MFM tip to locally boost a uniform external field set to 90% of an element's switching field have shown impressive initial results[16].

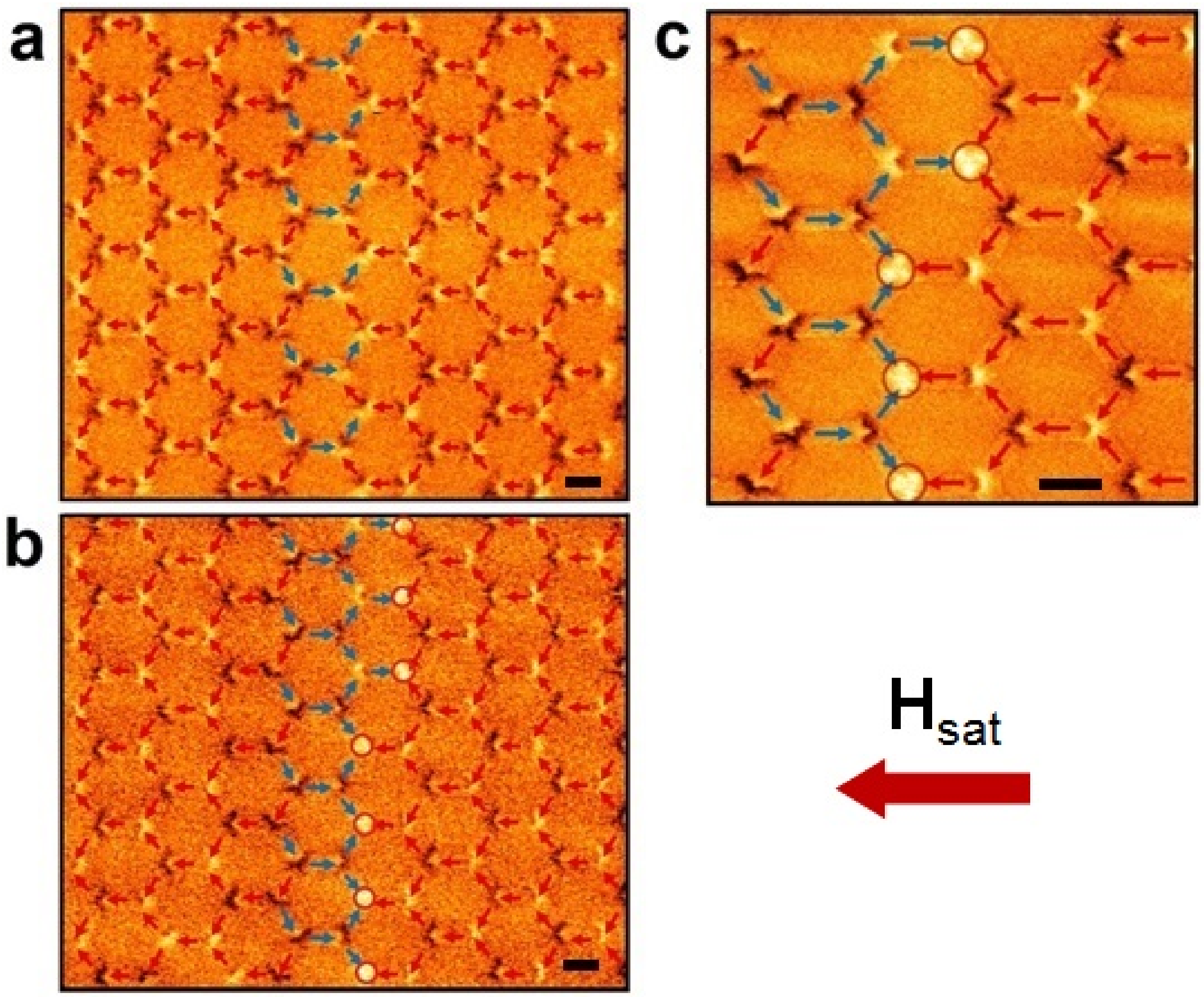

Figure S4: TMW-written states in ASI comprising 400 nm × 120 nm × 10 nm Py bars with 30 nm separations at vertices. TMW-switched bars (blue) are shown against a background of unwritten bars (red), initialised by a uniform external field. Scale bars are 400 nm long.

a) Initial TMW written state. An ordered column of reversed elements in a c-shape configuration is observed.

b) Subsequent TMW written state. Starting from the state shown in a), additional bars are reversed to create two columns of $+3\ q_m$ vertices, circled in red.

c) Magnified image of the central region of b).

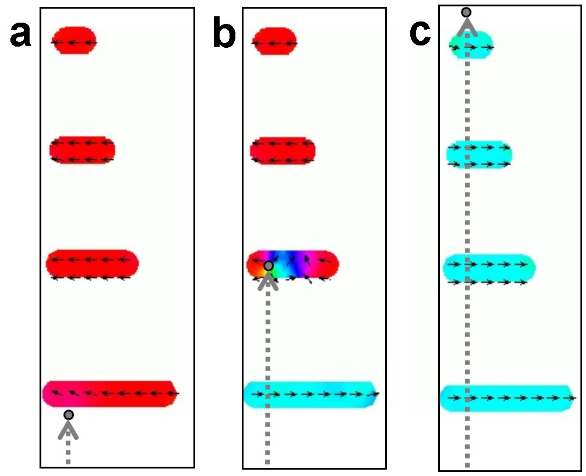

Figure S5: TMW reversal of 60 nm wide, 10 nm thick Py wires of 300 nm, 200 nm, 140 nm and 90 nm length. Grey arrow and circle represent the path and position of MFM tip respectively.

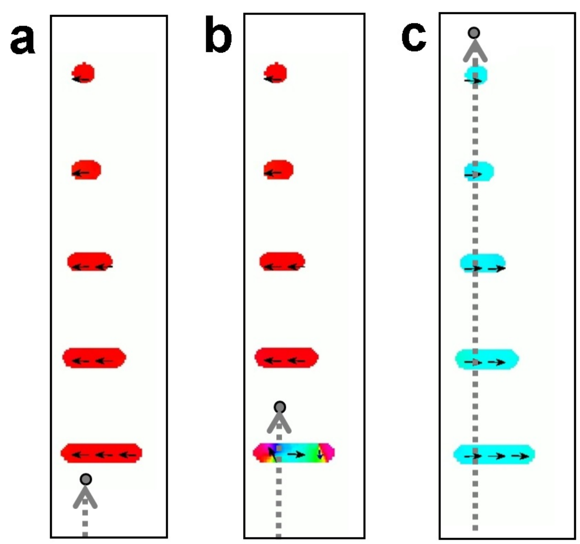

Figure S6: TMW reversal of 30 nm wide, 10 nm thick Py wires of 120 nm, 90 nm, 65 nm, 40 nm and 32 nm length. Grey arrow and circle represent the path and position of MFM tip respectively.

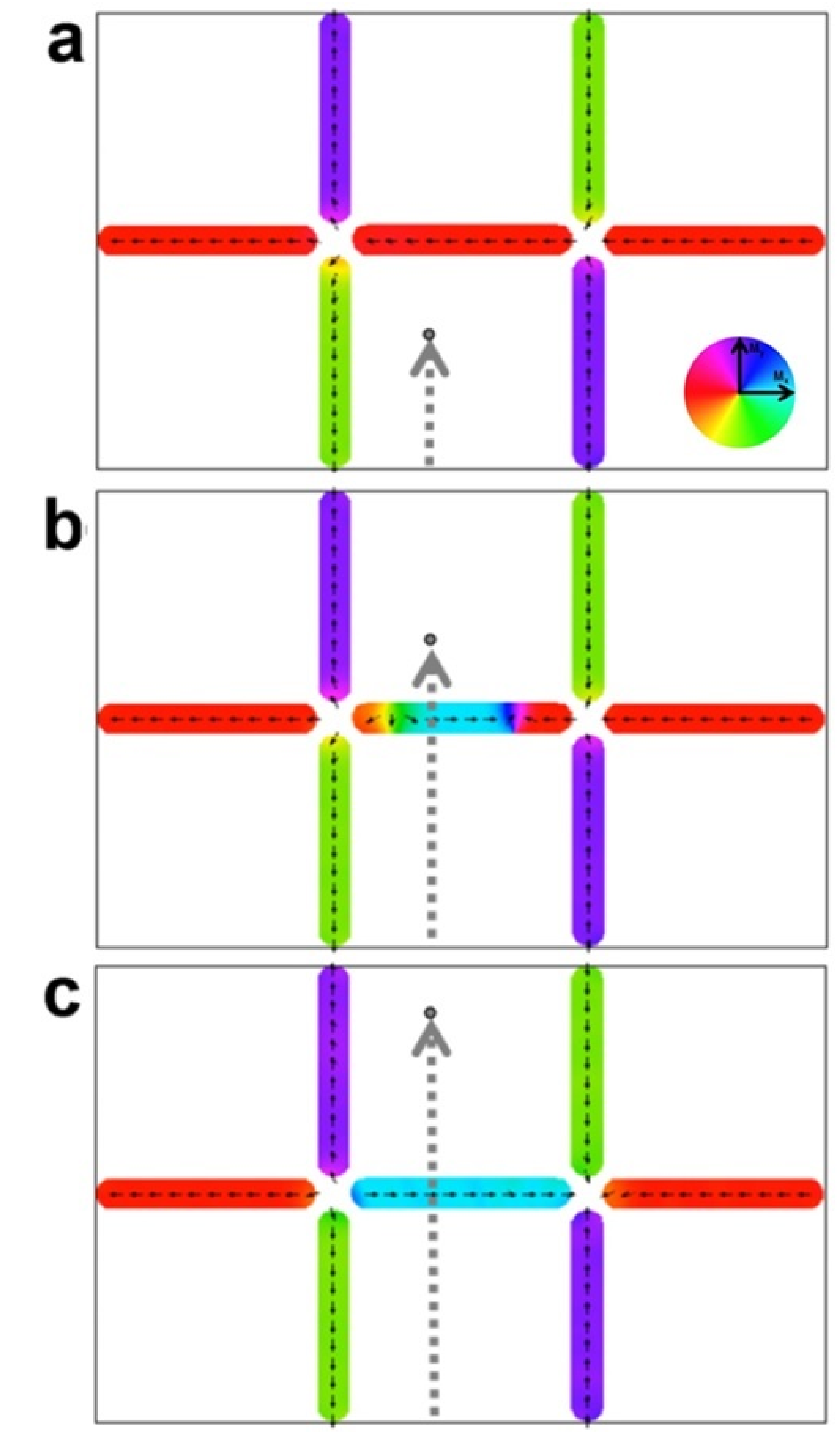

Figure S7: TMW writing of ± 4 q_m vertex states in square ASI comprising 400 nm × 60 nm × 10 nm Py bars. Grey arrow and circle represent the path and position of MFM tip respectively.

a) Initial magnetisation state.

b) Intermediary state with TMW-injected 180 ° DWs propagating through the central bar.

c) Final TMW-written state containing two pm 4 q_m vertices.

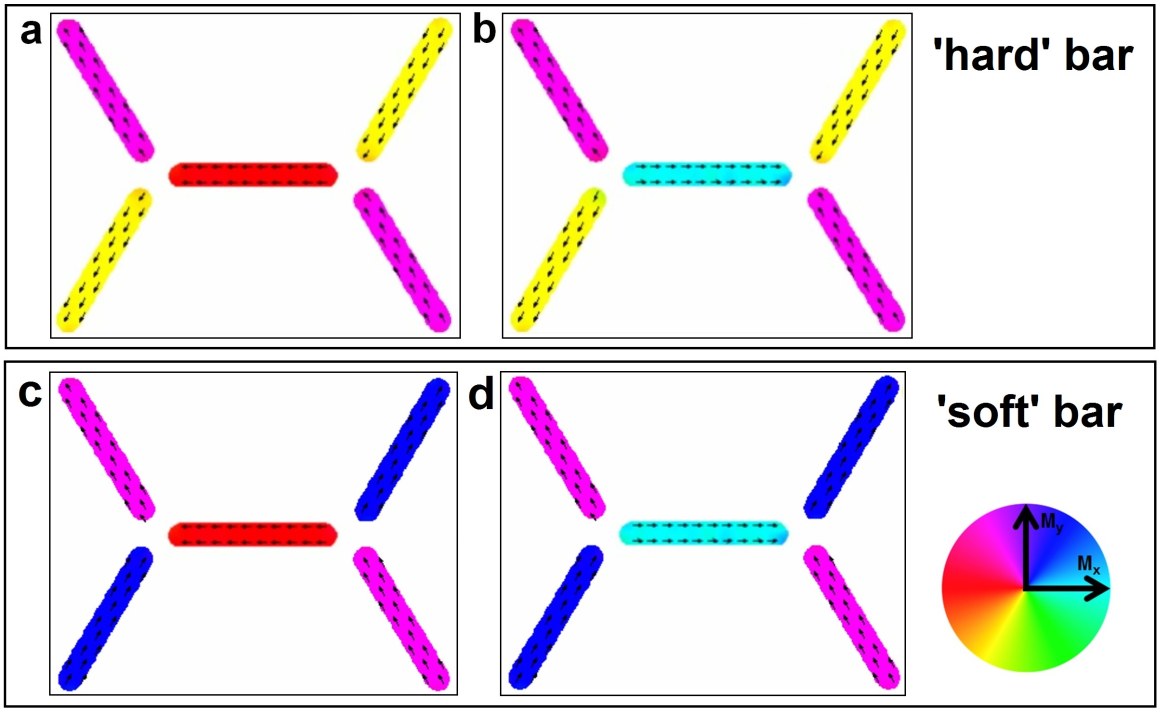

Figure S8: Switching events creating excited monopole-defect vertices (a-b) and non-excited vertices (c-d).
a-b) Switching of a 'hard' bar resulting in the creation of excited $\pm 3q_m$ vertices.
c-d) Switching of a 'soft' bar leaving non-excited vertices.

However, global field techniques have limited writing functionality in systems containing a distribution of switching fields, such as systems with elements of different spatial dimensions, different magnetic materials or strong inter-element interactions.

Typically, complete functional magnetic devices contain a range of different elements with a corresponding distribution of switching fields. For example, a global field tuned to 90% of a target element's switching field will reverse all elements with switching fields 10% lower than the target, ruling out selective switching for all but the softest elements. In strongly interacting systems, the switching field of an element is significantly modified by the magnetic states of its neighbouring elements. In such systems, bars that would create excited vertices when switched have substantially increased switching fields relative to bars creating non-excited vertices. We will refer to these bars as 'hard and 'soft respectively with switching examples shown in figure S8 a)-b) (hard) and c)-d) (soft). Below we demonstrate that global field based approaches are restricted to switching soft bars only, preventing access to the full microstate space. As technological progress necessitates that magnetic arrays operate at the highest possible densities, strong interactions between elements become unavoidable and competitive technologies must retain functionality in strongly interacting systems.

We performed micromagnetic simulations on the two-vertex kagome ASI configuration shown in figure S8 to quantify the range of switching fields in typical strongly and weakly interacting arrays. Bar dimensions of 400 nm X 60 nm X 10 nm were used and vertex separations giving strong (50 nm) and weak (300 nm) interactions. The system was initialised as in figure S8 a). Initially we start by forcing the 60° bars to remain fixed, to find the

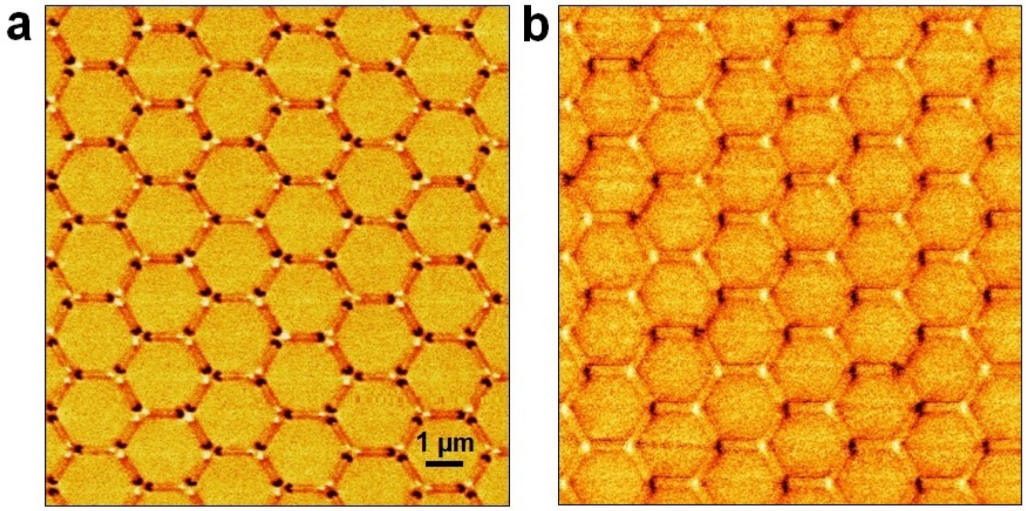

Figure S9: MFM images of as-grown ASI arrays.

a) Disconnected and **b)** connected ASI arrays immediately after deposition. The ice-rules are obeyed at every vertex indicating a strongly interacting system.

switching field of the hard central bar. We then relax that condition to find the switching field of the 60° bars. The process was then repeated for soft bars with the system initialised as in figure S8 c).

Hard bar switching fields	Central bar switching field	±60° bars switching field	Percentage difference	Difference in switching field
Strongly interacting case (50 nm gap)	97.5 mT	72.5 mT	26%	25 mT
Weakly interacting case (300 nm gap)	87.5 mT	72.5 mT	17%	15 mT
Single isolated bar	82.5 mT	NA	NA	NA

Soft bar switching fields	Central bar switching field	±60° bars switching field	Percentage difference	Difference in switching field
Strongly interacting case (50 nm gap)	84.5 mT	72.5 mT	14%	12 mT
Weakly interacting case (300 nm gap)	84.5 mT	72.5 mT	14%	12 mT
Single isolated bar	82.5 mT	NA	NA	NA

The tables above show the observed switching fields. It can be seen that for a strongly interacting system, the switching field of a hard bar is increased such that a global field tuned to 90% of its switching field will switch all soft bars in the system. As such, existing global field based techniques are seen to be inoperable in strongly interacting systems. Indeed as array densities increase, necessary for technological progress, the difference in switching field for hard bars will rise even higher[17] and supplying sufficient local field boosts without writing adjacent bars becomes an untenable proposition. As TMW operates on a distinctly different concept, directly manipulating topological defects to achieve controlled switching with no need for external global fields, the above issues do not apply as demonstrated by our TMW-writing of complex excited states in strongly-interacting systems.

6 Evidence of strong interactions in arrays studied in this work

To confirm that ASI arrays were in the strongly-interacting regime, structures were imaged via MFM immediately after deposition. In a randomly prepared non-interacting ASI system where the orientation of each macrospin is independent of its neighbours, the chance of observing no ±3 q_m monopole-defect vertices is given by the ratio of ice-rule obeying microstates $\frac{3}{\sqrt{2}}^N$, where N is the number of vertices, to the total number of microstates 2^{n} where n is the number of macrospins. A non-interacting 15 µm x 15 µm array containing 118 vertices and 222 macrospins therefore has a 2.1^{-11} probability of containing no ±3 q_m vertices. Figure S9 shows MFM images of disconnected (a) and connected (b) as-grown arrays with no ice-rule violations observed, showing structures are in the strongly-interacting ASI regime.

References

1. McMichael, R. & Donahue, M. Head to head domain wall structures in thin magnetic strips. *IEEE Trans. Magn.* **33**, 4167 (1997).

2. Gartside, J., Burn, D., Cohen, L. & Branford, W. A novel method for the injection and manipulation of magnetic charge states in nanostructures. *Scientific Reports* **6** (2016).

3. Döring, W. Über die trägheit der wände zwischen weißschen bezirken. *Zeitschrift für Naturforschung A* **3**, 373–379 (1948).

4. Tatara, G. & Kohno, H. Theory of current-driven domain wall motion: spin transfer versus momentum transfer. *Physical review letters* **92**, 086601 (2004).

5. Saitoh, E., Miyajima, H., Yamaoka, T. & Tatara, G. Current-induced resonance and mass determination of a single magnetic domain wall. *Nature* **432**, 203–206 (2004).

6. Hayward, T. *et al.* Pinning induced by inter-domain wall interactions in planar magnetic nanowires. *Applied Physics Letters* **96**, 052502 (2010).

7. Kittel, C. & Galt, J. Ferromagnetic domain theory. *Solid State Physics* **3**, 437–564 (1956).

8. Tchernyshyov, O. & Chern, G. W. Fractional vortices and composite domain walls in flat nanomagnets. *Phys. Rev. Lett.* **95**, 1–4 (2005). 0506744.

9. Pushp, A. *et al.* Domain wall trajectory determined by its fractional topological edge defects. *Nat. Phys.* **9**, 505 (2013).

10. Magiera, M. P., Hucht, A., Hinrichsen, H., Dahmen, S. R. & Wolf, D. E. Magnetic vortices induced by a moving tip. *EPL (Europhysics Letters)* **100**, 27004 (2012).

11. Magiera, M. P. & Schulz, S. Magnetic vortices induced by a monopole tip. *Magnetics, IEEE Transactions on* **50**, 1–4 (2014).

12. Gilbert, I. *et al.* Emergent reduced dimensionality by vertex frustration in artificial spin ice. *Nature Physics* **12**, 162 (2016).

13. Gilbert, I. *et al.* Emergent ice rule and magnetic charge screening from vertex frustration in artificial spin ice. *Nature Physics* **10**, 670 (2014).

14. Morrison, M. J., Nelson, T. R. & Nisoli, C. Unhappy vertices in artificial spin ice: new degeneracies from vertex frustration. *New Journal of Physics* **15**, 045009 (2013).

15. Chern, G.-W. & Mellado, P. Magnetic monopole polarons in spin ice with mixed coordination numbers. *arXiv preprint arXiv:1306.6154* (2013).

16. Wang, Y.-L. *et al.* Rewritable artificial magnetic charge ice. *Science* **352**, 962–966 (2016).

17. Fraleigh, R. D. *et al.* Characterization of switching field distributions in ising-like magnetic arrays. *Physical Review B* **95**, 144416 (2017).